LETTER

doi:10.1038/nature24030

Energetic eruptions leading to a peculiar hydrogen-rich explosion of a massive star

Iair Arcavi[1,2,3], D. Andrew Howell[1,3], Daniel Kasen[4,5,6], Lars Bildsten[2,3], Griffin Hosseinzadeh[1,3], Curtis McCully[1,3], Zheng Chuen Wong[1,3], Sarah Rebekah Katz[1,3], Avishay Gal-Yam[7], Jesper Sollerman[8], Francesco Taddia[8], Giorgos Leloudas[7,9], Christoffer Fremling[8], Peter E. Nugent[6,10], Assaf Horesh[7,11], Kunal Mooley[12], Clare Rumsey[13], S. Bradley Cenko[14,15], Melissa L. Graham[6,16], Daniel A. Perley[9,17], Ehud Nakar[18], Nir J. Shaviv[11], Omer Bromberg[18], Ken J. Shen[6], Eran O. Ofek[7], Yi Cao[16,19], Xiaofeng Wang[20], Fang Huang[20], Liming Rui[20], Tianmeng Zhang[21,22], Wenxiong Li[20], Zhitong Li[20], Jujia Zhang[23,24], Stefano Valenti[25], David Guevel[1,3], Benjamin Shappee[26], Christopher S. Kochanek[27,28], Thomas W.-S. Holoien[27,28], Alexei V. Filippenko[6,29], Rob Fender[12], Anders Nyholm[8], Ofer Yaron[7], Mansi M. Kasliwal[30], Mark Sullivan[31], Nadja Blagorodnova[30], Richard S. Walters[30], Ragnhild Lunnan[30], Danny Khazov[7], Igor Andreoni[32,33,34], Russ R. Laher[35], Nick Konidaris[26], Przemek Wozniak[36] & Brian Bue[37]

Every supernova so far observed has been considered to be the terminal explosion of a star. Moreover, all supernovae with absorption lines in their spectra show those lines decreasing in velocity over time, as the ejecta expand and thin, revealing slower-moving material that was previously hidden. In addition, every supernova that exhibits the absorption lines of hydrogen has one main light-curve peak, or a plateau in luminosity, lasting approximately 100 days before declining[1]. Here we report observations of iPTF14hls, an event that has spectra identical to a hydrogen-rich core-collapse supernova, but characteristics that differ extensively from those of known supernovae. The light curve has at least five peaks and remains bright for more than 600 days; the absorption lines show little to no decrease in velocity; and the radius of the line-forming region is more than an order of magnitude bigger than the radius of the photosphere derived from the continuum emission. These characteristics are consistent with a shell of several tens of solar masses ejected by the progenitor star at supernova-level energies a few hundred days before a terminal explosion. Another possible eruption was recorded at the same position in 1954. Multiple energetic pre-supernova eruptions are expected to occur in stars of 95 to 130 solar masses, which experience the pulsational pair instability[2–5]. That model, however, does not account for the continued presence of hydrogen, or the energetics observed here. Another mechanism for the violent ejection of mass in massive stars may be required.

On 2014 September 22.53 UT (universal time dates are used throughout), the Intermediate Palomar Transient Factory (iPTF) wide-field camera survey[6,7] discovered iPTF14hls at right ascension $\alpha_{J2000} = 09\,\mathrm{h}\,20\,\mathrm{min}\,34.30\,\mathrm{s}$ and declination $\delta_{J2000} = +50°\,41'\,46.8''$, at an R-band magnitude of 17.716 ± 0.033 (Extended Data Fig. 1). We have no observations of this position between 2014 May 28 and September 22, inducing an approximately 100-day uncertainty in the explosion time, so we use the discovery date as a reference epoch for all phases. We adopt a redshift of $z = 0.0344$, determined from narrow host-galaxy features, corresponding to a luminosity distance[9] of 156 Mpc.

On 2015 January 8, iPTF14hls was classified as a supernova of type II-P, on the basis of prominent, broad, Balmer series P Cygni lines in an optical spectrum[8]. So far, type II-P supernovae have been the only events ever observed to produce such spectra. In a type II-P supernova, the core of a massive star collapses to create a neutron star, sending a shock wave through the outer hydrogen-rich envelope and ejecting the envelope. The shock ionizes the ejecta, which later expand, cool and recombine. The photosphere follows the recombination front, which is at a roughly constant temperature ($T \approx 6{,}000$ K) as it makes its way inward in mass through the expanding ejecta[10] (that is, the photosphere is moving from material that is further out from the exploding star towards material that is further in, but the material inside the photosphere is expanding in the meantime). This leads to the approximately 100-day 'plateau' phase of roughly constant luminosity in the light curve and prominent hydrogen P Cygni features in the spectrum.

iPTF14hls, although identical to type II-P supernovae in its spectroscopic features, has several properties never before seen in a supernova. Instead of a 100-day plateau, the light curve of iPTF14hls lasts over 600 days and has at least five distinct peaks during which the luminosity varies by as much as 50% (Fig. 1). Blackbody fits to the broad-band

[1]Las Cumbres Observatory, Goleta, California 93117, USA. [2]Kavli Institute for Theoretical Physics, University of California, Santa Barbara, California 93106, USA. [3]Department of Physics, University of California, Santa Barbara, California 93106, USA. [4]Nuclear Science Division, Lawrence Berkeley National Laboratory, Berkeley, California 94720, USA. [5]Department of Physics, University of California, Berkeley, California 94720, USA. [6]Department of Astronomy, University of California, Berkeley, California 94720-3411, USA. [7]Department of Particle Physics and Astrophysics, The Weizmann Institute of Science, Rehovot 76100, Israel. [8]The Oskar Klein Centre, Department of Astronomy, Stockholm University, AlbaNova, SE-10691 Stockholm, Sweden. [9]Dark Cosmology Centre, Niels Bohr Institute, University of Copenhagen, Juliane Maries vej 30, 2100 Copenhagen, Denmark. [10]Computational Research Division, Lawrence Berkeley National Laboratory, Berkeley, California 94720, USA. [11]Racah Institute of Physics, The Hebrew University of Jerusalem, Jerusalem 91904, Israel. [12]Department of Physics, Astrophysics, University of Oxford, Denys Wilkinson Building, Oxford OX1 3RH, UK. [13]Astrophysics Group, Cavendish Laboratory, 19 J. J. Thomson Avenue, Cambridge CB3 0HE, UK. [14]Astrophysics Science Division, NASA Goddard Space Flight Center, Code 661, Greenbelt, Maryland 20771, USA. [15]Joint Space-Science Institute, University of Maryland, College Park, Maryland 20742, USA. [16]Department of Astronomy, University of Washington, Box 351580, Seattle, Washington 98195-1580, USA. [17]Astrophysics Research Institute, Liverpool John Moores University, IC2, Liverpool Science Park, 146 Brownlow Hill, Liverpool L3 5RF, UK. [18]The Raymond and Beverly Sackler School of Physics and Astronomy, Tel Aviv University, Tel Aviv 69978, Israel. [19]eScience Institute, University of Washington, Box 351570, Seattle, Washington 98195-1580, USA. [20]Physics Department and Tsinghua Center for Astrophysics, Tsinghua University, Beijing 100084, China. [21]Key Laboratory of Optical Astronomy, National Astronomical Observatories of China, Chinese Academy of Sciences, Beijing 100012, China. [22]School of Astronomy and Space Science, University of Chinese Academy of Sciences, Beijing 101408, China. [23]Yunnan Observatories, Chinese Academy of Sciences, Kunming 650011, China. [24]Key Laboratory for the Structure and Evolution of Celestial Objects, Chinese Academy of Sciences, Phoenix Mountain, East District, Kunming, Yunnan 650216, China. [25]Department of Physics, University of California, 1 Shields Avenue, Davis, California 95616, USA. [26]Carnegie Observatories, 813 Santa Barbara Street, Pasadena, California 91101, USA. [27]Department of Astronomy, The Ohio State University, 140 West 18th Avenue, Columbus, Ohio 43210, USA. [28]Center for Cosmology and AstroParticle Physics (CCAPP), The Ohio State University, 191 W. Woodruff Avenue, Columbus, Ohio 43210, USA. [29]Miller Institute for Basic Research in Science, University of California, Berkeley, California 94720, USA. [30]Cahill Center for Astrophysics, California Institute of Technology, Pasadena, California 91125, USA. [31]Department of Physics and Astronomy, University of Southampton, Southampton SO17 1BJ, UK. [32]Centre for Astrophysics and Supercomputing, Swinburne University of Technology, PO Box 218, Victoria 3122, Australia. [33]ARC Centre of Excellence for All-sky Astrophysics (CAASTRO), Australia. [34]Australian Astronomical Observatory. PO Box 915, North Ryde, New South Wales 1670, Australia. [35]Spitzer Science Center, California Institute of Technology, MS 314-6, Pasadena, California 91125, USA. [36]Space and Atmospheric Sciences Group, Mail Stop D466, Los Alamos National Laboratory, Los Alamos, New Mexico 87545, USA. [37]Jet Propulsion Laboratory, California Institute of Technology, Pasadena, California 91109, USA.

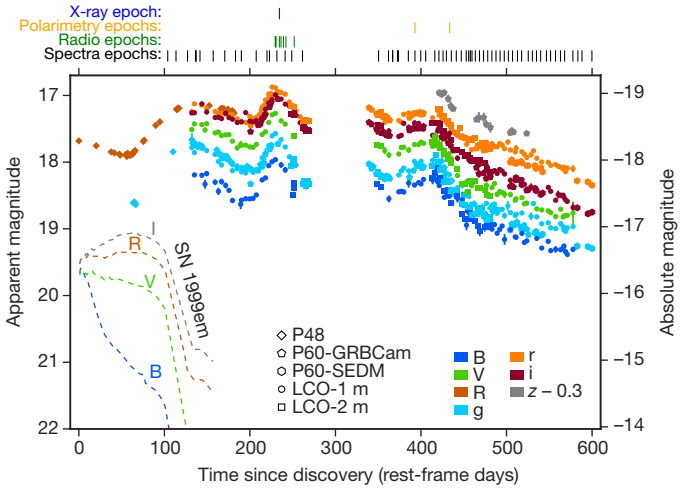

Figure 1 | Light curves of iPTF14hls. The type II-P supernova SN 1999em is shown in dashed lines[22], according to the ordinate axis at right. Data from the same day, instrument, and filter are averaged for clarity. The Spectral Energy Distribution Machine (SEDM) *i*-band data are shifted by +0.3 mag to compensate for filter differences. Unlike any known supernova, iPTF14hls has at least five distinct peaks in its light curve (at approximately 140 days, 220 days and 410 days after discovery, before discovery as indicated by the *R*-band light curve, and while it was behind the Sun between day 260 and day 340 after discovery). Error bars denote 1σ uncertainties.

optical *BVgi* photometry of iPTF14hls (see Methods) indicate a roughly constant effective temperature of 5,000–6,000 K, the same as the hydrogen-recombination temperature typically seen in type II-P supernovae. However, the inferred bolometric luminosity of a few times 10^{42} erg s^{-1} is at the high end of the range for typical type II-P supernovae[11], and the total radiated energy of $2.20^{+0.03}_{-0.05} \times 10^{50}$ erg emitted during the 450 days of our multi-band optical coverage is a few times larger than that of any known type II-P supernova. Given the uncertainty in the explosion time of iPTF14hls, the discrepancies with type II-P supernova timescales and energetics may be even larger.

The spectroscopic evolution of iPTF14hls is even harder to understand. It is a factor of approximately 10 slower than that of type II-P supernovae (Fig. 2); for example, the spectrum of iPTF14hls at 600 days looks like that of a normal type II-P supernova at 60 days (Extended Data Fig. 4). In all previously observed supernovae, the faster material is outside—spectra show a decrease of all measured velocities with time (by a factor of approximately 3 over 100 days) as the material expands and thins, and the photosphere moves inward in mass revealing deeper, slower-moving material. In iPTF14hls, velocities of hydrogen decline by only 25%, from 8,000 km s^{-1} to 6,000 km s^{-1} over 600 days, while the iron lines stay at a constant velocity of 4,000 km s^{-1} (Fig. 3).

It is usual to see hydrogen lines at higher velocities than iron lines owing to optical depth effects. But eventually, as the material expands and thins, hydrogen should be seen at lower velocity where the iron was previously seen (Extended Data Fig. 7). If the ejecta are expanding in size by a factor of approximately 6 between day 100 and day 600, in the absence of an additional energy source, an inward-moving photosphere scanning through the ejecta in velocity must occur.

An observation of constant velocity in a supernova can thus be caused by: (1) a central engine pushing material from the inside, sweeping the ejecta into a thin, dense shell[12,13], or (2) the spectral lines may correspond to ejecta that are far above the photosphere and detached from it. One-dimensional central-engine models compress

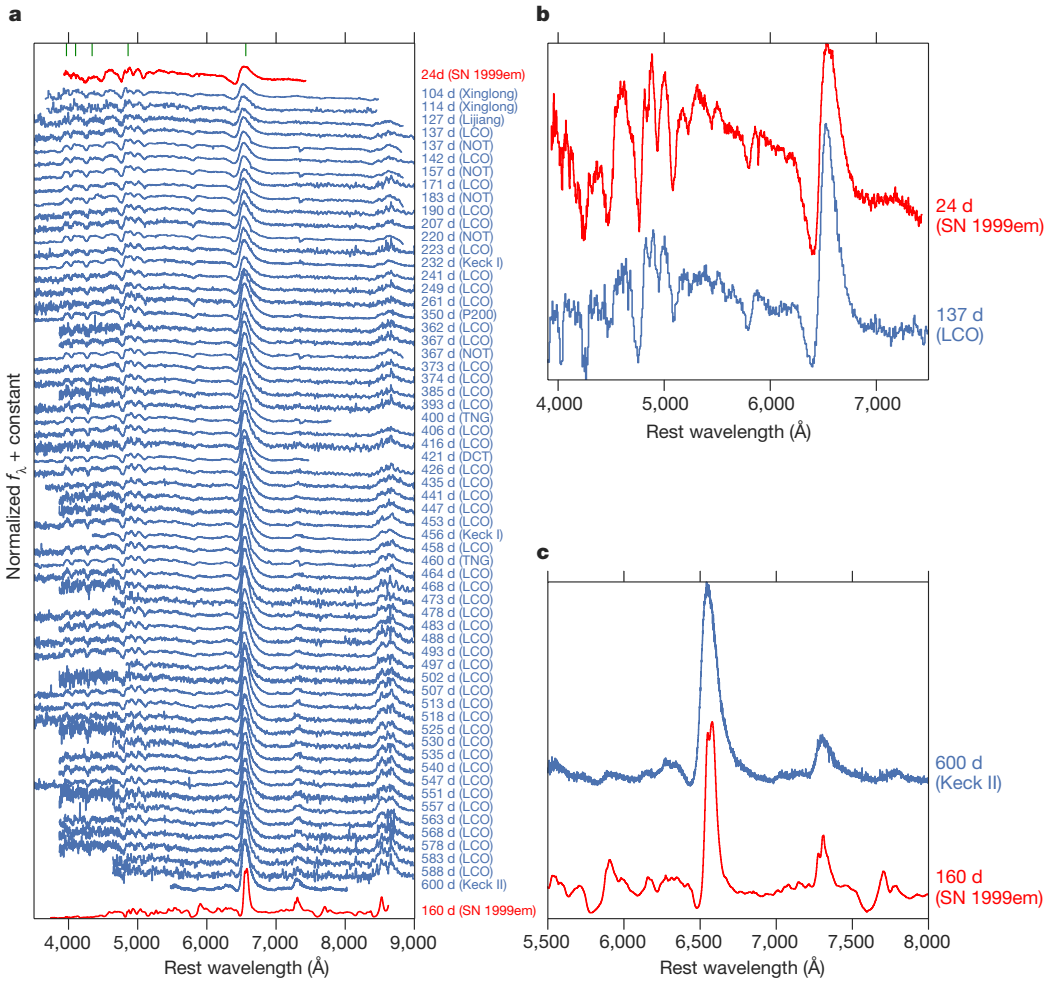

Figure 2 | Spectroscopic sequence of iPTF14hls. Our full sequence (**a**; blue) is shown with select spectra highlighted (**b**, **c**), in terms of normalized flux density as a function of rest-frame wavelength. The spectra are binned in wavelength and shifted in flux density for clarity. Phases are noted in rest-frame days since discovery, with the telescopes used in parentheses. Spectra of the type II-P supernova SN 1999em[22] (red) are shown with phases noted in rest-frame days since explosion. Balmer series hydrogen-line wavelengths are denoted in green (**a**). iPTF14hls is very similar spectroscopically to a type II-P supernova but evolves much more slowly. The spectral evolution is very smooth (**a**).

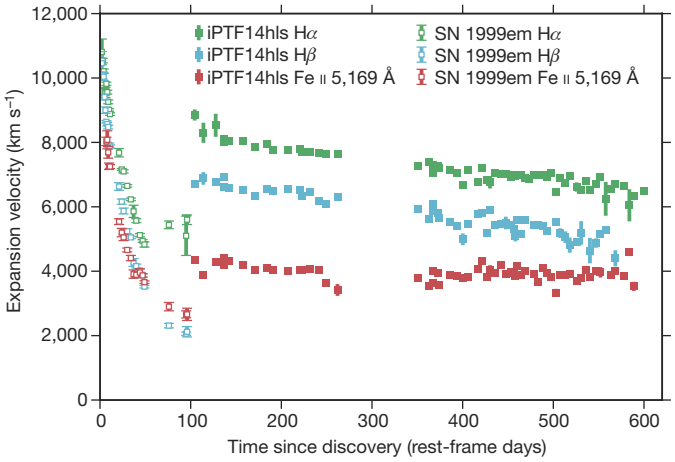

Figure 3 | Expansion velocities as a function of time. Velocities are measured from the P Cygni absorption component of three different spectral lines (see Methods) for iPTF14hls (filled symbols) and the prototypical type II-P supernova SN 1999em[22] (empty symbols). Error bars denote 1σ uncertainties for $n = 1{,}000$ samplings of the endpoints and are sometimes smaller than the marker size. The velocities seen for iPTF14hls evolve much more slowly compared with SN 1999em.

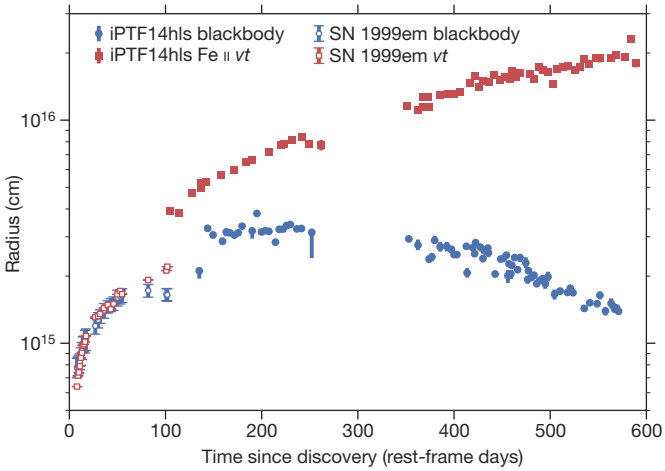

Figure 4 | The photospheric radius of iPTF14hls. The radius is estimated in two different ways: (1) using blackbody fits to the broad-band *BVgi* photometry (blue) and (2) using the derived expansion velocities of Fe II $\lambda = 5{,}169$ Å times the elapsed rest-frame time (*vt*) since discovery (red). The same quantities are shown for the type II-P supernova SN 1999em (empty symbols; after correcting for the blackbody dilution factor)[22]. Error bars denote 1σ uncertainties and are sometimes smaller than the marker size. For SN 1999em the radii overlap as expected, but for iPTF14hls they diverge, indicating that the line-forming region may be detached from the photosphere.

the iron and hydrogen lines to the same velocity, which is not the case for iPTF14hls (though multi-dimensional effects could alter this prediction). The spectral line evolution can more readily be explained if the lines are formed by ejecta from a prior eruption (that happened a few years before the discovery of iPTF14hls) that are detached from the continuum-emitting photosphere, which was formed in the terminal explosion (see Methods).

We estimate the position of the line-forming region to be *vt*, where *v* is the observed expansion velocity of the material at time *t*. For type II-P supernovae, this radius, when using the iron line velocities, is the same as the photospheric radius obtained by blackbody fits to the continuum emission, up to an order-unity "blackbody dilution factor"[14–16]. For iPTF14hls, the *vt*-inferred radius is instead larger than the blackbody-inferred radius by an order of magnitude on day 600 (Fig. 4). The fact that the two radii are so different from each other indicates that the line-forming region in iPTF14hls is indeed spatially detached from the continuum-emitting photosphere, in contrast to what is observed in all known type II-P supernovae.

The observations are thus consistent with the line-forming material being ejected in a massive and very energetic pre-supernova outburst, specifically in a shell of the order of a few tens of solar masses (see Methods). However, this requires a kinetic energy of about 10^{52} erg, normally associated with (or even exceeding that of) a supernova. Further evidence for a third, even earlier, explosion comes from an outburst of *R*-band magnitude $M_R \approx -15.6$ detected at the position of iPTF14hls in 1954 (formally a 2.2σ detection, though this is probably an underestimate owing to photographic nonlinearity; see Methods).

It is also unknown what is powering the light curve of iPTF14hls. Strong asymmetry may induce a luminosity increase in a particular direction. However, we do not detect any substantial polarization that would be indicative of asymmetry in the explosion (see Methods). Another energy source in iPTF14hls compared to normal type II-P supernovae could come from the interaction of the ejecta with previously ejected shells. However, in cases of supernovae interacting with dense circumstellar material, the interaction dominates the spectra in the form of a strong continuum together with broad, intermediate and narrow components of the Balmer emission lines[17,18]. None of these features is seen in the spectra of iPTF14hls (Fig. 2; Extended Data Fig. 5). We find no evidence of X-ray or radio emission (which are possible additional indicators of strong interaction)[19] in observations taken during the brightest peak of the optical light curve (see Methods). It is possible that any signs of interaction are being reprocessed by overlying, previously ejected material.

Either way, the progenitor of iPTF14hls probably experienced multiple energetic eruptions over the last decades of its life. Energetic eruptions are expected in stars with initial masses of about 95–130 solar masses, which undergo an instability arising from the production of electron–positron pairs[2]. Interactions between the different shells and/or the supernova ejecta and the shells can produce a variety of luminous long-lived transients with highly structured light curves[4,5] similar to that of iPTF14hls. Such pulsational pair instability supernovae are expected to occur in low-metallicity environments; indeed, iPTF14hls occurred on the outskirts of a low-mass, star-forming galaxy, possibly of low metal content (see Methods).

However, models of stars undergoing the pulsational pair instability eject most of the hydrogen envelope in the first eruption[5], whereas for iPTF14hls a few tens of solar masses of hydrogen were retained in the envelope after the 1954 outburst. Another problem is that pulsational pair instability models can account for up to about 4×10^{51} erg of kinetic energy in all eruptions together, while about 10^{52} erg are required just for the most recent eruption that ejected the line-forming region of iPTF14hls (see Methods).

iPTF14hls demonstrates that stars in the local Universe can undergo very massive eruptions in the decades leading to their collapse and yet, surprisingly, maintain a massive hydrogen-rich envelope for most of this period. Current models of massive star evolution and explosion need to be modified, or a completely new picture needs to be put forward, to account for the energetics of iPTF14hls, its lack of strong interaction signatures and the inferred amount of hydrogen it retained toward the end of its life.

Online Content Methods, along with any additional Extended Data display items and Source Data, are available in the online version of the paper; references unique to these sections appear only in the online paper.

Received 28 September 2016; accepted 16 August 2017.

1. Arcavi, I. Hydrogen-rich core-collapse supernova. In *Handbook of Supernovae* (eds Alsabti, A. W. & Murdin, P.) (in the press, Springer, 2016).
2. Barkat, Z., Rakavy, G. & Sack, N. Dynamics of supernova explosion resulting from pair formation. *Phys. Rev. Lett.* **18,** 379–381 (1967).
3. Heger, A. & Woosley, S. E. The nucleosynthetic signature of population III. *Astrophys. J.* **567,** 532–543 (2002).

4. Woosley, S. E., Blinnikov, S. & Heger, A. Pulsational pair instability as an explanation for the most luminous supernovae. *Nature* **450,** 390–392 (2007).
5. Woosley, S. E. Pulsational pair-instability supernovae. *Astrophys. J.* **836,** 244 (2017).
6. Law, N. M. *et al.* The Palomar Transient Factory: system overview, performance and first results. *Publ. Astron. Soc. Pacif.* **121,** 1395–1408 (2009).
7. Rau, A. *et al.* Exploring the optical transient sky with the Palomar Transient Factory. *Publ. Astron. Soc. Pacif.* **121,** 1334–1351 (2009).
8. Li, W., Wang, X. & Zhang, T. Spectroscopic classification of CSS141118:092034 +504148 as a type II-P supernova. *Astron. Telegr.* **6898** (2015).
9. The Planck Collaboration *et al.* Planck 2015 results. XIII. Cosmological parameters. *Astron. Astrophys.* **594,** A13 (2016).
10. Popov, D. V. An analytical model for the plateau stage of Type II supernovae. *Astrophys. J.* **414,** 712 (1993).
11. Bersten, M. C. & Hamuy, M. Bolometric light curves for 33 type II plateau supernovae. *Astrophys. J.* **701,** 200–208 (2009).
12. Kasen, D. & Bildsten, L. Supernova light curves powered by young magnetars. *Astrophys. J.* **717,** 245–249 (2010).
13. Dexter, J. & Kasen, D. Supernova light curves powered by fallback accretion. *Astrophys. J.* **772,** 30 (2013).
14. Kirshner, R. P. & Kwan, J. The envelopes of type II supernovae. *Astrophys. J.* **197,** 415 (1975).
15. Eastman, R. G., Schmidt, B. P. & Kirshner, R. The atmospheres of type II supernovae and the expanding photosphere method. *Astrophys. J.* **466,** 911 (1996).
16. Dessart, L. & Hillier, D. J. Distance determinations using type II supernovae and the expanding photosphere method. *Astron. Astrophys.* **439,** 671–685 (2005).
17. Schlegel, E. A new subclass of Type II supernovae? *Mon. Not. R. Astron. Soc.* **244,** 269–271 (1990).
18. Kiewe, M. *et al.* Caltech Core-Collapse Project (CCCP) observations of type IIn supernovae: typical properties and implications for their progenitor stars. *Astrophys. J.* **744,** 10 (2012).
19. Chevalier, R. A., Fransson, C. & Nymark, T. K. Radio and X-ray emission as probes of type IIP supernovae and red supergiant mass loss. *Astrophys. J.* **641,** 1029–1038 (2006).
20. Geha, M. *et al.* Variability-selected quasars in MACHO Project Magellanic cloud fields. *Astrophys. J.* **125,** 1–12 (2003).
21. Michel, F. C. Neutron star disk formation from supernova fall-back and possible observational consequences. *Nature* **333,** 644–645 (1988).
22. Leonard, D. C. *et al.* The distance to SN 1999em in NGC 1637 from the expanding photosphere method. *Publ. Astron. Soc. Pacif.* **114,** 35–64 (2002).

Supplementary Information is available in the online version of the paper.

Acknowledgements I. Arcavi is an Einstein Fellow. B.S. is a Hubble Fellow and a Carnegie-Princeton Fellow. A.V.F. is a Miller Senior Fellow. See the Supplementary Information for a full list of Acknowledgements.

Author Contributions I. Arcavi initiated the study, triggered follow-up observations, reduced data, performed the analysis and wrote the manuscript. D.A.H. is the Principal Investigator of the Las Cumbres Observatory (LCO) Supernova Key Project through which all of the LCO data were obtained; he also assisted with interpretation and the manuscript. D. Kasen and L.B. assisted with theoretical models, data interpretation, and with the manuscript. G.H. and C.McC. assisted with obtaining and reducing LCO data. Z.C.W. first flagged the supernova as interesting. S.R.K. performed the spectral expansion velocity measurements. A.G.-Y. is the Principal Investigator for core-collapse supernovae in iPTF and assisted with interpretation. J.S. and F.T. obtained the Nordic Optical Telescope spectra and polarimetry data and assisted with the manuscript. G.L. reduced the polarimetry data. C.F. reduced the Palomar 60-inch telescope (P60) data. P.E.N. discovered the 1954 eruption image of iPTF14hls, helped obtain the host-galaxy spectrum, and is a Co-Principal Investigator of the Keck proposal under which it and one of the supernova spectra were obtained. A.H. obtained and reduced the Very Large Array (VLA) data and is Principal Investigator of the programme through which the data were obtained. K.M. and C.R. obtained and reduced the Arcminute Microkelvin Imager Large Array (AMI-LA) data. S.B.C. obtained and reduced the Swift X-Ray Telescope (XRT) data. M.L.G. obtained and reduced Keck spectra. D.A.P. performed the host-galaxy analysis and assisted with the manuscript. E.N., O.B., N.J.S. and K.J.S. assisted with theoretical interpretation and the manuscript. E.O.O. helped with interpretation and the manuscript. Y.C. built the real-time iPTF image-subtraction pipeline and obtained Palomar 200-inch telescope (P200) observations. X.W., F.H., L.R., T.Z., W.L., Z.L. and J.Z. obtained and reduced the Xinglong, Lijiang, and Tsinghua University-NAOC telescope (TNT) data. S.V. built the LCO photometric and spectroscopic reduction pipelines and assisted with LCO observations, interpretation, and the manuscript. D.G. assisted with the Palomar Observatory Sky Survey (POSS) image analysis. B.S., C.S.K. and T.W.-S.H. obtained and reduced the All Sky Automated Survey for Supernovae (ASAS-SN) pre-discovery limits. A.V.F. is a Co-Principal Investigator of the Keck proposal under which the host-galaxy spectrum and one of the supernova spectra were obtained; he also helped with the manuscript. R.F. is Principal Investigator of the programme through which the AMI-LA data were obtained. A.N. helped scan for iPTF candidates and assisted with the manuscript. O.Y. is in charge of the iPTF candidate scanning effort. M.M.K. led the work for building iPTF. M.S. wrote the pipeline used to reduce Palomar 48-inch Oschin Schmidt telescope (P48) data. N.B. and R.S.W. obtained P60 SEDM photometry. R.L., D. Khazov, and I. Andreoni obtained P200 observations. R.R.L. contributed to building the P48 image-processing pipeline. N.K. was a main builder of the P60 SEDM. P.W. and B.B. helped build the machine-learning algorithms that identify iPTF supernova candidates.

Author Information Reprints and permissions information is available at www.nature.com/reprints. The authors declare no competing financial interests. Readers are welcome to comment on the online version of the paper. Publisher's note: Springer Nature remains neutral with regard to jurisdictional claims in published maps and institutional affiliations. Correspondence and requests for materials should be addressed to I. Arcavi (arcavi@gmail.com).

Reviewer Information *Nature* thanks P. Mazzali, S. Woosley and the other anonymous reviewer(s) for their contribution to the peer review of this work.

METHODS

Discovery. The intermediate Palomar Transient Factory (iPTF) first detected iPTF14hls on 2014 September 22.53 (Extended Data Fig. 1) using the iPTF real-time image-subtraction pipeline[23]. No source was seen at that position when it was previously visited by iPTF and by the All Sky Automated Survey for Supernovae (ASAS-SN)[24] on 2014 May 6.19 and 2014 May 20–28 down to 3σ limiting magnitudes of $R < 20.95$ and $V < 18.7$, respectively. The source was observed by iPTF again on 2014 October 13, October 31, November 4 and November 10 before being saved and given a name as part of routine iPTF transient scanning. On 2014 November 18, iPTF14hls was independently discovered by the Catalina Real-Time Transient Survey[25] as CSS141118:092034+504148, and later the event was reported to the Transient Name Server as AT 2016bse and Gaia16aog. On 2015 February 3, upon routine Las Cumbres Observatory (LCO) rescanning of previously saved iPTF candidates, we noticed the peculiar decline and subsequent rise of the light curve, and began an extensive campaign of spectroscopic and multi-band photometric follow-up observations.

Follow-up imaging. Follow-up imaging was obtained with the Palomar 48-inch Oschin Schmidt telescope (P48), the Palomar 60-inch telescope (P60)[26] using both the GRBCam and the SEDM instruments, the LCO[27] network 1-m and 2-m telescopes, and the 0.8-m Tsinghua University-NAOC telescope (TNT)[28] at the Xinglong Observatory. The TNT photometry is presented, together with Catalina Sky Survey (CSS; http://nesssi.cacr.caltech.edu/catalina/20141118/1411181490344143272.html) and Gaia (http://gsaweb.ast.cam.ac.uk/alerts/alert/Gaia16aog/) photometry downloaded from their respective websites, in Extended Data Figure 2. P48 images were first pre-processed by the Infrared Processing and Analysis Center (IPAC)[29]. Image subtraction and point-spread-function fitting were then performed[30] using pre-explosion images as templates. Magnitudes were calibrated to observations of the same field by the Sloan Digital Sky Survey (SDSS) DR10[31]. P60 images were pre-processed using a PyRAF-based pipeline[26]. Image subtraction, photometry extraction and calibration were performed with the FPipe pipeline[32] using SDSS images as references. LCO images were pre-processed using the Observatory Reduction and Acquisition Control Data Reduction pipeline (ORAC-DR)[33] up to 2016 May 4, and using the custom Python-based BANZAI pipeline afterward. Photometry was then extracted using the PyRAF-based LCOGTSNPipe pipeline[34] to perform point-spread-function fitting and calibration to the AAVSO Photometric All-Sky Survey[35] for *BV*-band data and SDSS DR8[36] for *gri*-band data. TNT images were reduced with standard Image Reduction and Analysis Facility (IRAF) routines; point-spread-function fitting was performed using the SNOoPy package and calibrated to the SDSS DR9[37] transformed to the Johnson system[38]. We correct all photometry for Milky Way extinction[39] extracted via the NASA Extragalactic Database. Pre-explosion non-detection limits are presented in Extended Data Figure 3.

We fitted a blackbody spectral energy distribution to every epoch of LCO photometry containing at least three of the *BVgi* filters obtained within 0.4 days of each other (we exclude *r*-band and *R*-band data from the fits owing to contamination from the Hα line). For each epoch we perform a blackbody fit using Markov Chain Monte Carlo simulations through the Python emcee package[40] to estimate the blackbody temperature and radius at the measured distance to iPTF14hls of 156 Mpc.

Follow-up spectroscopy. Spectra of iPTF14hls were obtained with the Floyds instrument mounted on the northern LCO 2-m telescope[27], the Andalucia Faint Object Spectrograph and Camera (ALFOSC) mounted on the 2.5-m Nordic Optical Telescope (NOT), the Device Optimized for the LOw RESolution (DOLoRes) mounted on the 3.6-m Telescopio Nazionale Galileo (TNG), the Low Resolution Imaging Spectrometer (LRIS)[41] mounted on the Keck-I 10-m telescope, the DEep Imaging Multi-Object Spectrograph (DEIMOS)[42] mounted on the Keck-II 10-m telescope, the Double Beam Spectrograph (DBSP)[43] mounted on the Palomar 200-inch telescope (P200), the Beijing Faint Object Spectrograph and Camera (BFOSC) on the Xinglong 2.16-m telescope of the National Astronomical Observatories of China, the Yunnan Faint Object Spectrograph and Camera (YFOSC) on the Lijiang 2.4-m telescope of the Yunnan Observatories, and the DeVeny spectrograph mounted on the 4.3-m Discovery Channel Telescope (DCT). The Floyds spectra were reduced using the PyRAF-based floydsspec pipeline. The ALFOSC and DOLORES spectra were reduced using custom MATLAB pipelines. The LRIS spectra were reduced using the IDL LPipe pipeline. The DEIMOS spectrum was reduced using a modified version of the DEEP2 pipeline[44,45] combined with standard PyRAF and IDL routines for trace extraction, flux calibration and telluric correction. The DBSP spectrum was reduced using custom IRAF and IDL routines. The BFOSC, YFOSC and DeVeny spectra were reduced using standard IRAF procedures. No Na I D line absorption is seen at the redshift of the host galaxy, indicating very low host-galaxy extinction at the supernova position.

We fitted each iPTF14hls spectrum to a library of type II supernovae (which includes a full set of SN 1999em spectra[22]) using Superfit[47]. We then calculate the average best-fitting supernova phase, weighing all the possible fits by their corresponding fit scores. We repeat this process for cutouts of the iPTF14hls spectra centred around the Hα, Hβ and Fe II $\lambda = 5{,}169$ Å features (separately). The weighted-average best-fit phases for each cutout are presented in Extended Data Figure 4. iPTF14hls can be seen to evolve more slowly than other type II supernovae by a factor of approximately 10 when considering the entire spectrum, as well as when considering the Hβ and the Fe II $\lambda = 5{,}169$ Å features separately, and by a factor of 6–7 when considering the Hα emission feature separately.

Expansion velocities for different elements in iPTF14hls were measured by fitting a parabola around the minimum of the absorption feature of their respective P Cygni profiles. The difference between the minimum of the best-fit parabola and the rest wavelength of the line was translated to an expansion velocity. The endpoints of each parabolic fit were chosen manually for each line, so that they would remain the same for all spectra. Uncertainties in the velocities were estimated by randomly varying these endpoints 1,000 times by ± 5 Å around their original values.

iPTF14hls is probably not powered by interaction. As mentioned in the main text, interaction between supernova ejecta and pre-existing, dense circumstellar material could cause an increase in luminosity. However, iPTF14hls does not display the spectral line profiles typically seen in such cases (Extended Data Fig. 5).

In some interaction models the collision of the supernova ejecta and the circumstellar material occurs outside the broad-line-forming region, diluting the line emission. Focusing on the approximately 50% luminosity increase of iPTF14hls between rest-frame day 207 and day 232 after discovery (Fig. 1), we find that the spectra taken on day 207 and day 232 are identical up to a global normalization factor. This indicates that the increase in luminosity is equal at all wavelengths, in contrast to the expected line dilution from interaction (Extended Data Fig. 6).

Additional possible indicators of interaction are strong X-ray and/or radio emission. We observed the location of iPTF14hls with the X-Ray Telescope (XRT)[48] onboard the Swift satellite[49] on 2015 May 23.05. A total of 4.9 ks of live exposure time was obtained on the source. We use online analysis tools[50,51] to search for X-ray emission at the location of iPTF14hls. No source is detected with an upper limit on the 0.3–10.0-keV count rate of $< 2.3 \times 10^{-3}$ counts s^{-1}. Assuming a power-law spectrum with a photon index of $\Gamma = 2$ and a Galactic H column density[52] of 1.4×10^{20} cm^{-2}, this corresponds to an upper limit on the unabsorbed 0.3–10.0-keV flux of $f_X < 8.4 \times 10^{-14}$ erg cm^{-2} s^{-1}. At the luminosity distance of iPTF14hls this corresponds to a luminosity limit of $L_X < 2.5 \times 10^{41}$ erg s^{-1} (which is roughly 10^{-2} of the peak bolometric luminosity). The lack of X-ray emission disfavours strong interaction in iPTF14hls, though some interacting supernovae display X-ray emission fainter than the limit we deduce here[53].

We observed iPTF14hls also with the Arcminute Microkelvin Imager Large Array (AMI-LA)[54] at 15 GHz on 2015 May 18.59, May 19.77, May 23.63, May 25.65, May 28.66, and May 31.62. Quasars 3C48 and J2035+1056 were used as the flux/bandpass and phase calibrators, respectively. Radio frequency interference excision and calibration of the raw data were done with a fully automated pipeline AMI-REDUCE[55,56]. The calibrated data for the supernova were imported into CASA (Common Astronomy Software Applications) and imaged independently for each epoch into 512×512 pixel maps (4″ per pixel) using the clean task. A similar imaging scheme was used for the concatenated data from all the epochs as well. The supernova was not detected on any of the individual epochs, with 3σ upper limits of 60–120 μJy. The combined 3σ upper limit is 36 μJy. There is a 5%–10% absolute flux calibration uncertainty that we have not considered in these upper limits. On 2016 June 10, iPTF14hls was observed with the VLA at 6.1 GHz. The VLA data were reduced using standard CASA software routines where J0920+4441 and 3C286 were used as phase and flux calibrators. No radio emission was observed at the supernova position to a 3σ upper limit of 21.3 μJy. At the luminosity distance of iPTF14hls, this corresponds to 6.2×10^{26} erg s^{-1} Hz^{-1}, which is fainter than the radio emission of most interacting supernovae[53]. We conclude that iPTF14hls does not show any of the signatures normally seen in supernovae powered by interaction.

A possible central-engine power source for iPTF14hls. A central engine such as the spindown of a magnetar[12,57,58] or fallback accretion onto a black hole[13,59] created after core collapse (assuming the material falling back has sufficient angular momentum to form a disk) could inject power to the supernova, although (as noted in the main text) this may fail to reproduce the observed iron and hydrogen line velocity difference. A magnetar (with an initial spin period of about 5–10 ms and a magnetic field of about $(0.5–1) \times 10^{14}$ G) could produce the observed average luminosity and timescale of iPTF14hls[12]. However, the analytical magnetar light curve required to fit the late-time decline overpredicts the early-time emission of iPTF14hls (Extended Data Fig. 2) and produces a smooth rather than variable light curve[12,13].

For a black-hole central engine, on the other hand, instabilities in the accretion flow might produce strong light-curve variability, as seen in active galactic nuclei[20].

In this case, the light curve is expected to eventually settle onto a $t^{-5/3}$ decline rate[21] after the last instability. Such a decline rate is indeed observed for iPTF14hls starting around day 450 (Extended Data Fig. 2), supporting a black-hole power source. We conclude that iPTF14hls does not show the expected signatures of magnetar power (using available analytical models), but might be consistent with black-hole accretion power.

No signs of asymmetry in iPTF14hls. A possible explanation for the high luminosities and apparent emitted energy of iPTF14hls, as well as the discrepancy between its line-forming versus blackbody radii, is strong asymmetry in the explosion. Such asymmetry would be indicated by a polarization signal.

We observed iPTF14hls with the Andalucia Faint Object Spectrograph and Camera (ALFOSC) mounted on the 2.5-m Nordic Optical Telescope (NOT) in polarimetric mode on 2015 November 03 in the *R* band, and on December 15 in the *V* band (we also obtained observations on 2015 October 28 and November 14 but we discard them because of very poor observing conditions). We used a 1/2-wave plate in the FAPOL unit (the polarimeter unit in the Filter And Shutter Unit, FASU) and a calcite plate mounted in the aperture wheel, and observed at four different retarder angles (0°, 22.5°, 45°, 67.5°). The data were reduced in a standard manner, using bias frames and flat fields without the polarization units in the light path. The field of view contains one bright star that can be used for calibration and for determining the interstellar polarization in the Galaxy. The low Galactic extinction towards iPTF14hls implies an expected interstellar polarization value[60] of $<0.13\%$.

To measure the fluxes we performed aperture photometry, and to compute the polarisation we followed standard procedures[61]. For our epoch with the best signal-to-noise (2015 November 03), we measure $P = 0.40\% \pm 0.27\%$ for iPTF14hls and $P = 0.17\% \pm 0.09\%$ for the comparison star, in agreement with the interstellar polarization prediction. These results suggest that iPTF14hls is close to spherically symmetric, similar to what is observed for type II-P supernovae during their plateau phase[62]. The 2015 December 15 epoch yields a lower precision ($P = 1.1\% \pm 0.7\%$ for iPTF14hls and $P = 0.80\% \pm 0.23\%$ for the comparison star), but is still consistent with very low asphericity.

Expansion velocities of iPTF14hls. In a supernova, the ejecta are in homologous expansion—that is, the radius of the ejecta at time t evolves as $r = vt$, with faster material at larger radii. Even for perfectly mixed ejecta, at any given time, spectral lines of different elements form in different regions. Specifically, the iron (Fe) lines are formed at smaller radii than the hydrogen (H) lines and therefore display a lower velocity. This is also the case in iPTF14hls. As time passes and the ejecta expand and recombine, the line-forming region of each element moves inward in mass to a region where the outflow is slower. This is why, normally, the velocity of all lines is observed to decrease with time. Thus, following the line velocity over a wide range of time (and hence mass coordinates) provides a 'scan' of the velocity profile over a large range of the ejecta. Although different lines are formed in different regions, all line-forming regions scan the velocity profile of the same ejecta. Therefore, if there is a large velocity gradient in the ejecta, we expect to see both a large velocity difference between the Fe and H lines as well as considerable evolution in the velocity of each line as the material expands. These two features are seen clearly in the typical case of SN 1999em (Extended Data Fig. 7). However, this is not the case in iPTF14hls. On the one hand, there is a large difference between the H and Fe line velocities, indicating a large velocity gradient in the ejecta. On the other hand, the velocity of each line shows almost no evolution in time between day 100 and day 600 after discovery. If the line-forming material were ejected at the time of discovery, then this time span corresponds to a change by a factor of about 6 in radius. In this case, the lack of observed velocity evolution indicates a very shallow velocity gradient in the ejecta, which is inconsistent with the large velocity difference between the lines. However, if the ejection of the line-forming material took place before discovery, then the relative change in radius during the observations is small, indicating that the position of the line-forming region does not change much, potentially solving the apparent contradiction.

The line-forming region of iPTF14hls. The nearly constant line velocities measured in iPTF14hls suggest that the lines form in a massive shell, perhaps ejected prior to the explosion. Here we estimate the mass and energetics required for such a shell to produce the observed line features.

Consider a uniform shell of mass M with a radius r and width Δr. The number density of hydrogen atoms in the shell is:

$$n_{\rm H} = \frac{Y_{\rm H} M}{\mu m_{\rm p} 4\pi r^2 \Delta r} \tag{1}$$

where $Y_{\rm H} \approx 0.9$ is the number fraction of hydrogen and $\mu \approx 1.34$ is the mean atomic mass for solar gas ($m_{\rm p}$ is the proton mass). In a rapidly expanding, homologous outflow ejected at a time $t_{\rm ej}$, the strength of a spectral line is characterized by the Sobolev optical depth approximation:

$$\tau_{\rm Sob} = \frac{\pi e^2}{m_e c} n_{\rm l} f t_{\rm ej} \lambda_0 \tag{2}$$

where $n_{\rm l}$ is the number density of atoms in the lower level, f is the line oscillation strength, $t_{\rm ej}$ is the time since explosion, m_e is the mass of the electron and λ_0 is the line rest wavelength. For a line to produce a noticeable absorption component in the spectra, it must have $\tau_{\rm Sob} \gtrsim 1$.

To estimate the populations in the lower level of the line transition (for the Balmer series this is the $n = 2$ level), we apply the nebular approximation[63], which assumes that the mean intensity of the radiation field at a radius above a nearly blackbody photosphere is $J_\nu(r) = W(r) B_\nu(T_{\rm bb})$, where B_ν is the Planck function, $T_{\rm bb}$ is the temperature of the photosphere, and $W(r)$ is the geometrical dilution factor of the radiation field:

$$W(r) = \frac{1}{2}\left[1 - \sqrt{1 - r_{\rm p}^2/r^2}\right] \approx \frac{r_{\rm p}^2}{4r^2} \tag{3}$$

Here, $r_{\rm p}$ is the photospheric radius and the last expression assumes $r \gg r_{\rm p}$. For a two-level atom subject to this radiation field, the number density in the $n = 2$ excited state is:

$$n_2 \approx n_1 W \frac{g_2}{g_1} e^{-\Delta E_{1,2}/kT} \tag{4}$$

where (n_1, n_2) and (g_1, g_2) are, respectively, the number density and statistical weights of the $n = 1$ and $n = 2$ levels, and $\Delta E_{1,2}$ is the energy difference between the levels.

Since essentially all of the hydrogen in the shell will be neutral and in the ground state, $n_1 \approx n_{\rm H}$. The Sobolev optical depth is then:

$$\tau_{\rm H\alpha} \approx \left[\frac{\pi e^2}{m_e c} f \lambda_0 t_{\rm ej}\right] \frac{Y_{\rm H} M}{\mu m_{\rm p}} \frac{r_{\rm p}^2}{16\pi r^4 \Delta r} \frac{g_2}{g_1} e^{-\Delta E_{1,2}/kT} \tag{5}$$

Using $g_1 = 2$, $g_2 = 8$, $\Delta E_{1,2} = 10.2$ eV, $\lambda_0 = 6{,}563$ Å (for the Hα transition), and $f = 0.64$, and taking $T = 6{,}500$ K, $\Delta r = \Delta v t_{\rm ej}$, and $r = v t_{\rm ej}$ gives

$$\tau_{\rm H\alpha} \approx 0.96 \left[\frac{M}{45 M_\odot}\right] \left[\frac{600\ {\rm days}}{t_{\rm ej}}\right]^4 \left[\frac{r_{\rm p}}{1.5 \times 10^{15}\ {\rm cm}}\right]^2 \left[\frac{6{,}000\ {\rm km\ s^{-1}}}{v}\right]^4 \left[\frac{1{,}000\ {\rm km\ s^{-1}}}{\Delta v}\right] \tag{6}$$

(where $M_\odot$ is the solar mass). Though approximate, this argument demonstrates that a shell with a mass of the order of a few tens of solar masses is probably required for producing Balmer absorption lines throughout the approximately 600-day duration of the iPTF14hls light curve. The corresponding kinetic energy of the outburst is about 10^{52} erg. In the case where the shell was ejected before the first iPTF14hls observations, the mass and energy required would increase. However, the mass required to associate the line-forming region with the 1954 eruption would be about $10^7 M_\odot$, and hence not reasonable, implying that the line-forming region was ejected in a separate, more recent, eruption.

For comparison, the electron-scattering optical depth of the shell is:

$$\tau_{\rm es} = n_{\rm H} x_{\rm H\,II}\ \sigma_{\rm T} \Delta r \approx 0.77 x_{\rm H\,II} \left[\frac{M}{45 M_\odot}\right] \left[\frac{600\ {\rm days}}{t_{\rm ej}}\right]^2 \left[\frac{6{,}000\ {\rm km\ s^{-1}}}{v}\right]^4 \tag{7}$$

where $\sigma_{\rm T}$ is the Thomson cross-section and $x_{\rm H\,II}$ is the fraction of ionized hydrogen. The shell will be largely neutral ($x_{\rm H\,II} \ll 1$), because the region where the radiation field is sufficient to ionize hydrogen occurs at the photosphere ($r_{\rm p}$) where the recombination front forms. The shell radius is much larger than $r_{\rm p}$, so the radiation field is strongly diluted. Thus, while the shell can form line features, it will be optically thin in the continuum and allow most of the pseudo-blackbody continuum from the photosphere to pass through.

The velocity of 6,000 km s^{-1} seen for Hα at day 600 after discovery is also seen for Hβ at day 200 after discovery. If we calculate the optical depth (see equation (5)) for Hβ (plugging in the parameters for day $200 + t_0$, where t_0 is the offset between the ejection of the shell and discovery) and equate it to that of Hα at day $600 + t_0$, then we can solve for the ejection time t_0, assuming that the optical depths for Hα and Hβ were the same when each was observed at 6,000 km s^{-1}, and that the entire shell was ejected simultaneously. Using $\lambda_0 = 4{,}861$ Å and $f = 0.12$ for the Hβ transition, we find $t_0 \approx 100$–200 days (the main source of error is the uncertainty in the precise temperature difference between the two epochs), meaning that the line-forming shell was ejected 100–200 days before discovery. We have deep non-detection limits for part of this epoch (Extended Data Fig. 3), suggesting that the

ejection of the shell could have been a low-luminosity event. This estimation of the ejection time, however, relies on many simplifying assumptions, so it should be considered only as an approximation.

A historical outburst at the position of iPTF14hls. The Palomar Observatory Sky Survey (POSS)[64] observed the field of iPTF14hls on 1954 February 23 in the blue and red filters. POSS-II[65] then re-observed the field on 1993 January 2 in the blue filter and on 1995 March 30 in the red filter. We obtained these images through the STScI Digitized Sky Survey and we find a source at the position of iPTF14hls in the blue image from POSS that is not present in the blue image from POSS-II (Extended Data Fig. 8). We do not see this source in either of the red images, but they are not as deep as the blue images (the limiting magnitude is roughly 20 for the red images compared to 21.1 for the blue images)[64].

We register the POSS blue image to the POSS-II blue image using the IRAF task wregister. We then use the apphot package in PyRAF, with a 3-pixel aperture, to measure the flux in six stars in the field near the position of iPTF14hls to determine a zero-point offset for the two images. We find an offset of 0.132 ± 0.050 mag. We then perform the same measurement around the nucleus of the host galaxy of iPTF14hls and find an offset of 0.141 mag, consistent with the zero-point offset. Next we perform the same aperture photometry measurement at the position of iPTF14hls in both images. We find a magnitude difference of 0.31 ± 0.14 over the host-galaxy level confirming the presence of an outburst in the 1954 image at the position of iPTF14hls at a 2.2σ confidence level. Owing to the nonlinear nature of the photographic plates used in the two POSS surveys, as well as differences between the filters[65], we cannot perform meaningful image subtraction between the POSS epochs to obtain more accurate photometric measurements. We consider this confidence level to be a conservative estimate; the outburst can be seen clearly by eye in the images (Extended Data Fig. 8).

We calibrate the six stars used for the zero-point comparison to SDSS *u*-band plus *g*-band fluxes (the POSS blue filter roughly covers the SDSS *u* and *g* bands)[64] and find that the magnitude of the 1954 outburst (after removing the host-galaxy contribution) is $20.4 \pm 0.1(\text{stat}) \pm 0.8(\text{sys})$. The first error is statistical and due to photometric measurement uncertainties, while the second error is systematic and caused by the calibration to SDSS (the large error value is probably produced by filter and detector differences between POSS and SDSS).

This corresponds to an absolute magnitude for the outburst of approximately −15.6 at the luminosity distance of iPTF14hls (this is only a lower limit on the peak luminosity of the eruption, as we have only one epoch of observations). Such an eruption may be produced by the pulsational pair instability[2–5]. Eruptions of similar luminosity (though probably caused by different instabilities) are inferred to be common in type IIn supernova progenitors in the last year prior to explosion[66]. Spectra and broad-band colours are available for three such possible outbursts—a precursor to PTF10bjb[66], PTF13efv (a precursor to SNHunt275)[67] and the first 2012 outburst of SN2009ip[68]—all of which display rather flat continuum emission, consistent with the limited colour information we have for the 1954 outburst of iPTF14hls (that is, the red nondetection limit being about 0.4 magnitudes brighter than the blue detection).

Given the host galaxy size of about 10–100 times the centroiding error of the outburst, and a typical supernova rate of about 1/100 per galaxy per year, there is a probability of a few per cent that the detected outburst is an unrelated supernova that happened to occur at the position of iPTF14hls.

The rate of iPTF14hls-like events. On 2014 November 18, iPTF14hls was independently discovered by the Catalina Real-Time Transient Survey[25] as CSS141118:092034+504148, and more recently the event was reported to the Transient Name Server as AT 2016bse and Gaia16aog. The fact that it was discovered multiple times, but dismissed as a run-of-the-mill type II-P supernova, suggests that similar events may have been missed in the past. We ourselves would not have noticed the unique properties of iPTF14hls had the iPTF survey scheduler not automatically continued to monitor the position of iPTF14hls. In addition, if iPTF14hls-like events are limited to low-mass galaxies, then targeted transient surveys would have missed them completely.

To our knowledge, iPTF14hls is the only supernova ever discovered to show such long-lived, slowly evolving type II-P-like emission. The PTF and iPTF surveys discovered 631 type II supernovae, indicating that iPTF14hls-like events could be about 10^{-3}–10^{-2} of the type II supernova rate. Since luminous, long-lived varying events could be easier to detect in transient surveys compared to normal supernovae, the true volumetric rate of iPTF14hls-like events could be much lower. On the other hand, we cannot rule out whether such events were discovered in the past but dismissed as normal type II-P supernovae after one spectrum with no subsequent follow-up observations or as possible active galactic nuclei owing to the light curve behaviour. It is therefore not possible to calculate a precise rate for iPTF14hls-like events based on this single discovery, but whatever the explosion channel, it is likely to be rare. Even so, the Large Synoptic Survey Telescope could find hundreds of iPTF14hls-like events in its decade-long survey of the transient sky (and more if iPTF14hls-like events are more common in the early Universe, as is indicated by the possible low-metallicity environment of iPTF14hls).

The host galaxy of iPTF14hls. We obtained a spectrum of the host galaxy of iPTF14hls on 2015 December 11 with the Low Resolution Imaging Spectrometer (LRIS)[41] mounted on the Keck-I 10-m telescope. The spectrum was reduced using standard techniques optimized for Keck+LRIS by the CarPy package in PyRAF, and flux calibrated with spectrophotometric standard stars obtained on the night of our observations in the same instrument configuration. The host-galaxy spectrum, which is available for download via WISeREP[46], shows clear detections of Hα, Hβ, [O II] $\lambda = 3{,}727$ Å and [O III] $\lambda = 4{,}958$ Å and 5,007 Å, which we use to determine a redshift of 0.0344. A faint detection of [N II] $\lambda = 6{,}583$ Å is also possible, but the feature is difficult to confirm because the continuum is contaminated by broad Hα emission from the nearby supernova. All of the lines are weak (equivalent width <20 Å) and no other lines are strongly detected. We extracted the fluxes of all lines by fitting Gaussians to their profiles (Extended Data Table 1), and calculated the metallicity by fitting[69] the line-strength ratios using several different diagnostics and calibrations (Extended Data Table 2). We find a range of metallicity estimates of $12 + \log(\text{O/H}) = 8.3$–$8.6$, corresponding to about (0.4–0.9)$Z_\odot$ (where $Z_\odot$ is the solar metallicity)[70]. A low metallicity could help explain how the progenitor of iPTF14hls retained a very massive hydrogen envelope. Future, more direct environment studies will be able to better probe the metallicity at the explosion site.

We fitted the SDSS *ugriz* photometry of the host galaxy[71] with standard spectral energy distribution fitting techniques[72] using the BC03[73] stellar population synthesis models. Assuming a metallicity of $0.5Z_\odot$, the best-fit total stellar mass is $(3.2 \pm 0.5) \times 10^8 M_\odot$, similar to that of the Small Magellanic Cloud.

Data availability. The photometric data that support the findings of this study are available in the Open Supernova Catalog[81], https://sne.space/sne/iPTF14hls/. The spectroscopic data that support the findings of this study are available on the Weizmann Interactive Supernova data REPository (WISeREP)[46], https://wiserep.weizmann.ac.il/, and on the Open Supernova Catalog. Source Data for Figs 1, 3 and 4, and for Extended Data Figures 2, 3 and 4 are provided with the online version of the paper.

23. Cao, Y., Nugent, P. E. & Ka sliwal, M. M. Intermediate Palomar Transient Factory: realtime image subtraction pipeline. *Publ. Astron. Soc. Pacif.* **128,** 114502 (2016).
24. Shappee, B. J. *et al.* The man behind the curtain: X-rays drive the UV through NIR variability in the 2013 active galactic nucleus outburst in NGC 2617. *Astrophys. J.* **788,** 48 (2014).
25. Drake, A. J. *et al.* First results from the Catalina Real-time Transient Survey. *Astrophys. J.* **696,** 870–884 (2009).
26. Cenko, S. B. *et al.* The Automated Palomar 60 Inch Telescope. *Publ. Astron. Soc. Pacif.* **118,** 1396–1406 (2006).
27. Brown, T. M. *et al.* Las Cumbres Observatory Global Telescope Network. *Publ. Astron. Soc. Pacif.* **125,** 1031–1055 (2013).
28. Huang, F. *et al.* The photometric system of the Tsinghua-NAOC 80-cm telescope at NAOC Xinglong Observatory. *Res. Astron. Astrophys.* **12,** 1585–1596 (2012).
29. Laher, R. R. *et al.* IPAC image processing and data archiving for the Palomar Transient Factory. *Publ. Astron. Soc. Pacif.* **126,** 674–710 (2014).
30. Sullivan, M. *et al.* Photometric selection of high-redshift type Ia supernova candidates. *Astron. J.* **131,** 960–972 (2006).
31. Ahn, C. P. *et al.* The tenth data release of the Sloan Digital Sky Survey: first spectroscopic data from the SDSS-III Apache Point Observatory Galactic Evolution Experiment. *Astrophys. J. Suppl. Ser.* **211,** 17 (2014).
32. Fremling, C. *et al.* PTF12os and iPTF13bvn. Two stripped-envelope supernovae from low-mass progenitors in NGC 5806. *Astron. Astrophys.* **593,** A68 (2016).
33. Jenness, T. & Economou, F. ORAC-DR: a generic data reduction pipeline infrastructure. *Astron. Comput.* **9,** 40–48 (2015).
34. Valenti, S. *et al.* The diversity of Type II supernova versus the similarity in their progenitors. *Mon. Not. R. Astron. Soc.* **459,** 3939–3962 (2016).
35. Henden, A. A., Welch, D. L., Terrell, D. & Levine, S. E. The AAVSO Photometric All-Sky Survey (APASS). *Am. Astron. Soc. Meet. Abstr.* **214,** 407.02 (2009).
36. Aihara, H. *et al.* The eighth data release of the Sloan Digital Sky Survey: first data from SDSS-III. *Astrophys. J. Suppl. Ser.* **193,** 29 (2011).
37. Ahn, C. P. *et al.* The ninth data release of the Sloan Digital Sky Survey: first spectroscopic data from the SDSS-III Baryon Oscillation Spectroscopic Survey. *Astrophys. J. Suppl. Ser.* **203,** 21 (2012).
38. Chonis, T. S. & Gaskell, C. M. Setting UBVRI photometric zero-points using Sloan Digital Sky Survey ugriz magnitudes. *Astrophys. J.* **135,** 264–267 (2008).
39. Schlafly, E. F. & Finkbeiner, D. P. Measuring reddening with SDSS stellar spectra and recalibrating SFD. *Astrophys. J.* **737,** 103 (2011).
40. Foreman-Mackey, D., Hogg, D. W., Lang, D. & Goodman, J. emcee: the MCMC hammer. *Publ. Astron. Soc. Pacif.* **125,** 306–312 (2013).
41. Oke, J. B. *et al.* The Keck Low-Resolution Imaging Spectrometer. *Publ. Astron. Soc. Pacif.* **107,** 375 (1995).
42. Faber, S. M. *et al.* in *Instrument Design and Performance for Optical/Infrared Ground-based Telescopes* (eds Iye, M. & Moorwood, A. F. M.) *Proc. SPIE* **4841,** 1657–1669 (2003).

43. Oke, J. B. & Gunn, J. E. An efficient low resolution and moderate resolution spectrograph for the Hale telescope. *Publ. Astron. Soc. Pacif.* **94,** 586 (1982).
44. Cooper, M. C., Newman, J. A., Davis, M., Finkbeiner, D. P., & Gerke, B. F. spec2d: DEEP2 DEIMOS Spectral Pipeline. *Astrophysics Source Code Library* ascl:1203.003 (2012).
45. Newman, J. A. *et al.* The DEEP2 galaxy redshift survey: design, observations, data reduction, and redshifts. *Astrophys. J.* **208,** 5 (2013).
46. Yaron, O. & Gal-Yam, A. WISeREP—an interactive supernova data repository. *Publ. Astron. Soc. Pacif.* **124,** 668–681 (2012).
47. Howell, D. A. *et al.* Gemini spectroscopy of supernovae from SNLS: improving high redshift SN selection and classification. *Astrophys. J.* **634,** 1190–1201 (2005).
48. Burrows, D. N. *et al.* The Swift X-ray telescope. *Space Sci. Rev.* **120,** 165–195 (2005).
49. Gehrels, N. *et al.* The Swift gamma-ray burst mission. *Astrophys. J.* **611,** 1005–1020 (2004).
50. Evans, P. A. *et al.* An online repository of Swift/XRT light curves of GRBs. *Astron. Astrophys.* **469,** 379–385 (2007).
51. Evans, P. A. *et al.* Methods and results of an automatic analysis of a complete sample of Swift-XRT observations of GRBs. *Mon. Not. R. Astron. Soc.* **397,** 1177–1201 (2009).
52. Willingale, R., Starling, R. L. C., Beardmore, A. P., Tanvir, N. R. & O'Brien, P. T. Calibration of X-ray absorption in our Galaxy. *Mon. Not. R. Astron. Soc.* **431,** 394–404 (2013).
53. Margutti, R. *et al.* Ejection of the massive hydrogen-rich envelope timed with the collapse of the stripped SN2014C. *Astrophys. J.* **835,** 140 (2017).
54. Zwart, J. T. L. *et al.* The Arcminute Microkelvin Imager. *Mon. Not. R. Astron. Soc.* **391,** 1545–1558 (2008).
55. Davies, M. L. *et al.* Follow-up observations at 16 and 33 GHz of extragalactic sources from WMAP 3-year data: I—spectral properties. *Mon. Not. R. Astron. Soc.* **400,** 984–994 (2009).
56. Perrott, Y. C. *et al.* AMI galactic plane survey at 16 GHz: I—observing, mapping and source extraction. *Mon. Not. R. Astron. Soc.* **429,** 3330–3340 (2013).
57. Ostriker, J. P. & Gunn, J. E. On the nature of pulsars. I. Theory. *Astrophys. J.* **157,** 1395 (1969).
58. Woosley, S. E. Bright supernovae from magnetar birth. *Astrophys. J.* **719,** L204–L207 (2010).
59. Colgate, S. A. Neutron-star formation, thermonuclear supernovae, and heavy-element reimplosion. *Astrophys. J.* **163,** 221 (1971).
60. Serkowski, K., Mathewson, D. L. & Ford, V. L. Wavelength dependence of interstellar polarization and ratio of total to selective extinction. *Astrophys. J.* **196,** 261 (1975).
61. Patat, F. & Romaniello, M. Error analysis for dual-beam optical linear polarimetry. *Publ. Astron. Soc. Pacif.* **118,** 146–161 (2006).
62. Leonard, D. C. & Filippenko, A. V. Spectropolarimetry of the type II supernovae 1997ds, 1998A, and 1999gi. *Publ. Astron. Soc. Pacif.* **113,** 920–936 (2001).
63. Abbott, D. C. & Lucy, L. B. Multiline transfer and the dynamics of stellar winds. *Astrophys. J.* **288,** 679 (1985).
64. Minkowski, R. L. & Abell, G. O. The National Geographic Society—Palomar Observatory Sky Survey. In *Basic Astronomical Data: Stars and Stellar Systems* (ed. Strand, K. A.) 481–487 (Univ. Chicago Press, 1963).
65. Reid, I. N. *et al.* The second Palomar Sky Survey. *Publ. Astron. Soc. Pacif.* **103,** 661 (1991).
66. Ofek, E. O. *et al.* Precursors prior to type IIn supernova explosions are common: precursor rates, properties, and correlations. *Astrophys. J.* **789,** 104 (2014).
67. Ofek, E. O. *et al.* PTF13efv: an outburst 500 days prior to the SNHunt 275 explosion and its radiative efficiency. *Astrophys. J.* **824,** 6 (2016).
68. Fraser, M. *et al.* SN 2009ip a la PESSTO: no evidence for core-collapse yet. *Mon. Not. R. Astron. Soc.* **433,** 1312–1337 (2013).
69. Bianco, F. B. *et al.* Monte Carlo method for calculating oxygen abundances and their uncertainties from strong-line flux measurements. *Astron. Comput.* **16,** 54–66 (2016).
70. Asplund, M., Grevesse, N., Sauval, A. J. & Scott, P. The chemical composition of the Sun. *Annu. Rev. Astron. Astrophys.* **47,** 481–522 (2009).
71. Alam, S. *et al.* The eleventh and twelfth data releases of the Sloan Digital Sky Survey: final data from SDSS-III. *Astrophys. J. Suppl. Ser.* **219,** 12 (2015).
72. Perley, D. A. *et al.* A population of massive, luminous galaxies hosting heavily dust-obscured gamma-ray bursts: implications for the use of GRBs as tracers of cosmic star formation. *Astrophys. J.* **778,** 128 (2013).
73. Bruzual, G. & Charlot, S. Stellar population synthesis at the resolution of 2003. *Mon. Not. R. Astron. Soc.* **344,** 1000–1028 (2003).
74. Nagao, T., Maiolino, R. & Marconi, A. Gas metallicity diagnostics in star-forming galaxies. *Astron. Astrophys.* **459,** 85–101 (2006).
75. Denicoló, G., Terlevich, R. & Terlevich, E. New light on the search for low metallicity galaxies I. The N_2 calibrator. *Mon. Not. R. Astron. Soc.* **330,** 69–74 (2002).
76. Pettini, M. & Pagel, B. E. J. [O III]/[N II] as an abundance indicator at high redshift. *Mon. Not. R. Astron. Soc.* **348,** L59–L63 (2004).
77. Maiolino, R. *et al.* AMAZE. I. The evolution of the mass-metallicity relation at $z>3$. *Astron. Astrophys.* **488,** 463–479 (2008).
78. Marino, R. A. *et al.* The O_3N_2 and N_2 abundance indicators revisited: improved calibrations based on CALIFA and Te-based literature data. *Astron. Astrophys.* **559,** A114 (2013).
79. Kobulnicky, H. A. & Kewley, L. J. Metallicities of 0.3. *Astrophys. J.* **617,** 240–261 (2004).
80. Kewley, L. J. & Dopita, M. A. Using strong lines to estimate abundances in extragalactic H ii regions and starburst galaxies. *Astrophys. J. Suppl. Ser.* **142,** 35–52 (2002).
81. Guillochon, J. *et al.* An open catalog for supernova data. *Astrophys. J.* **835,** 64 (2017).

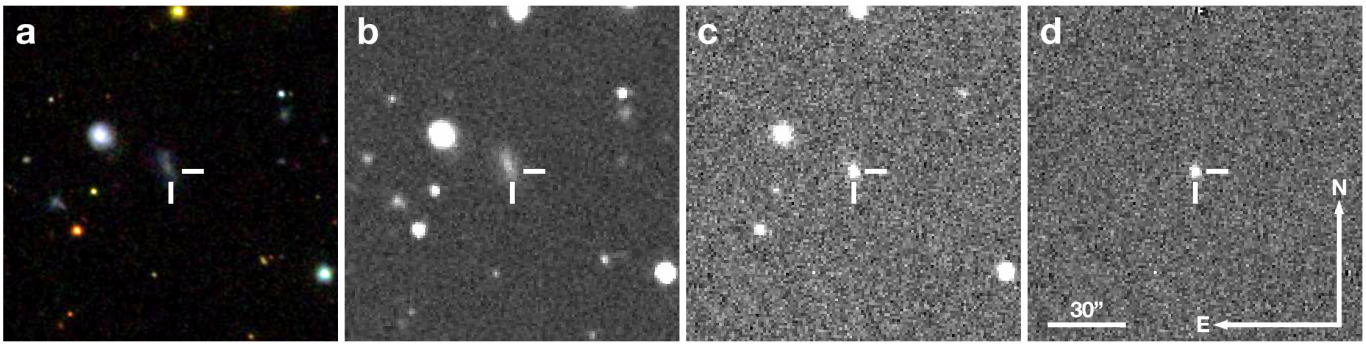

Extended Data Figure 1 | The discovery and environment of iPTF14hls. **a**, SDSS image centered at the position of iPTF14hls. **b**, Palomar 48-inch deep coadded pre-discovery reference image. **c**, Palomar 48-inch discovery image of iPTF14hls. **d**, The result of subtracting the reference image from the discovery image. The position of iPTF14hls is indicated by tick marks in each image.

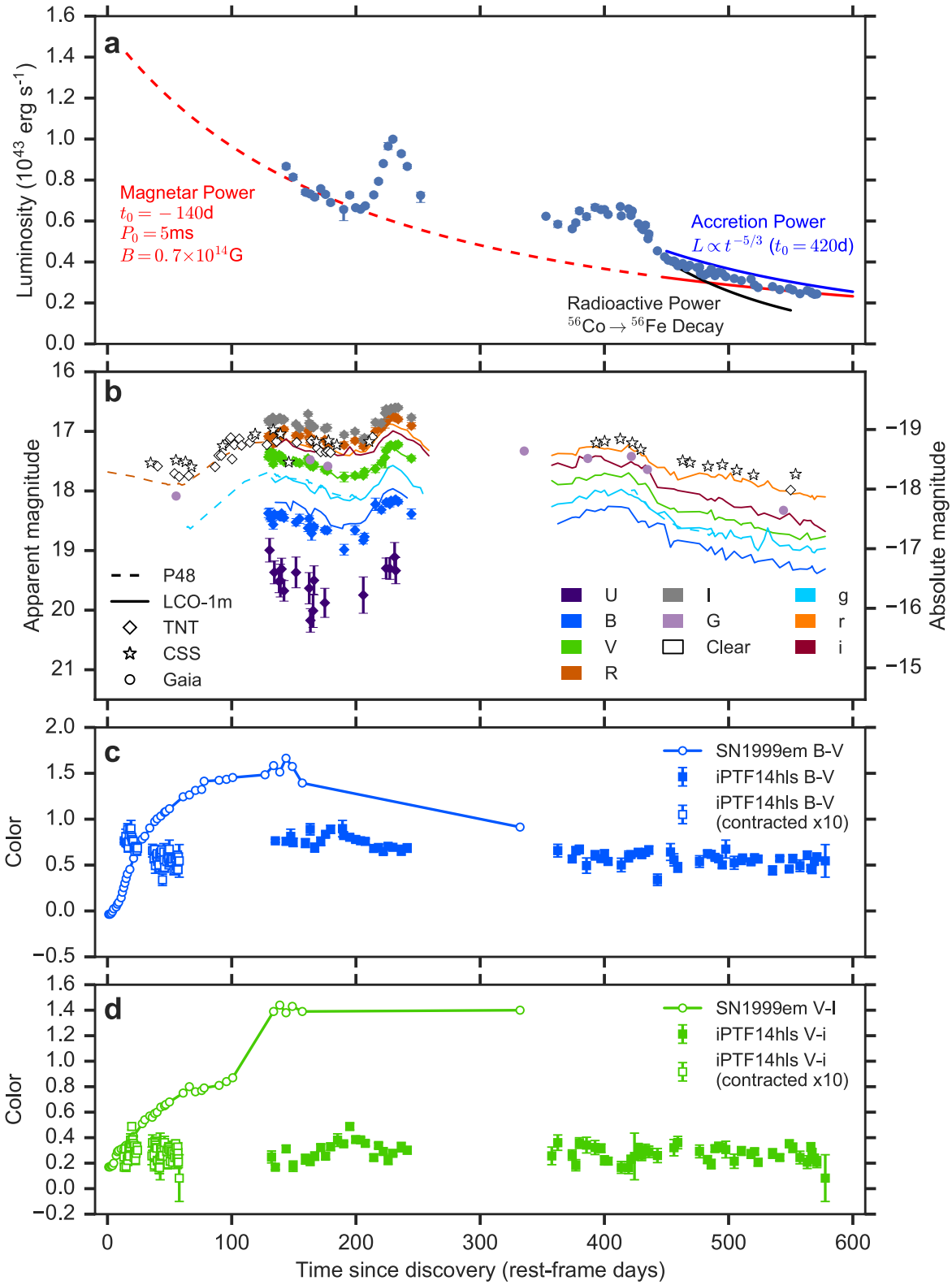

Extended Data Figure 2 | Additional photometry of iPTF14hls. The bolometric light curve of iPTF14hls (**a**) deduced from the blackbody fits shows a late-time decline rate that is slower than the radioactive decay of ^{56}Co (black), but consistent with both delayed accretion power (blue; t_0 is the onset of accretion at the last peak which could represent a final fallback event) and magnetar spindown power (red; t_0 is the formation time of the magnetar, P_0 is the initial spin period and B is the magnetic field in this simple analytic model). The magnetar model, however, is not consistent with the luminosity during the first 100 days, as implied by the P48, CSS and Gaia observations (**b**), unless the early-time magnetar emission is substantially adiabatically degraded. TNT photometry of iPTF14hls and publicly available CSS photometry (retrieved from the CSS website) and Gaia photometry (retrieved from the Gaia Alerts website) not presented in Fig. 1 are shown in **b**. Data from the P48 (dashed lines) and the LCO 1-m telescope (solid lines) presented in Fig. 1 are shown for comparison. Photometric points from the same day, instrument and filter are averaged for clarity. The $B-V$ (**c**) and $V-I/i$ (**d**) colour evolution of iPTF14hls from the LCO 1-m data (filled squares) differs from that of the normal type II-P SN 1999em (empty circles)[22], even when contracting the iPTF14hls data by a factor of 10 in time (empty squares) to compensate for the slow evolution observed in its spectra compared to that of normal type II-P supernovae. All error bars, when available, denote 1σ uncertainties.

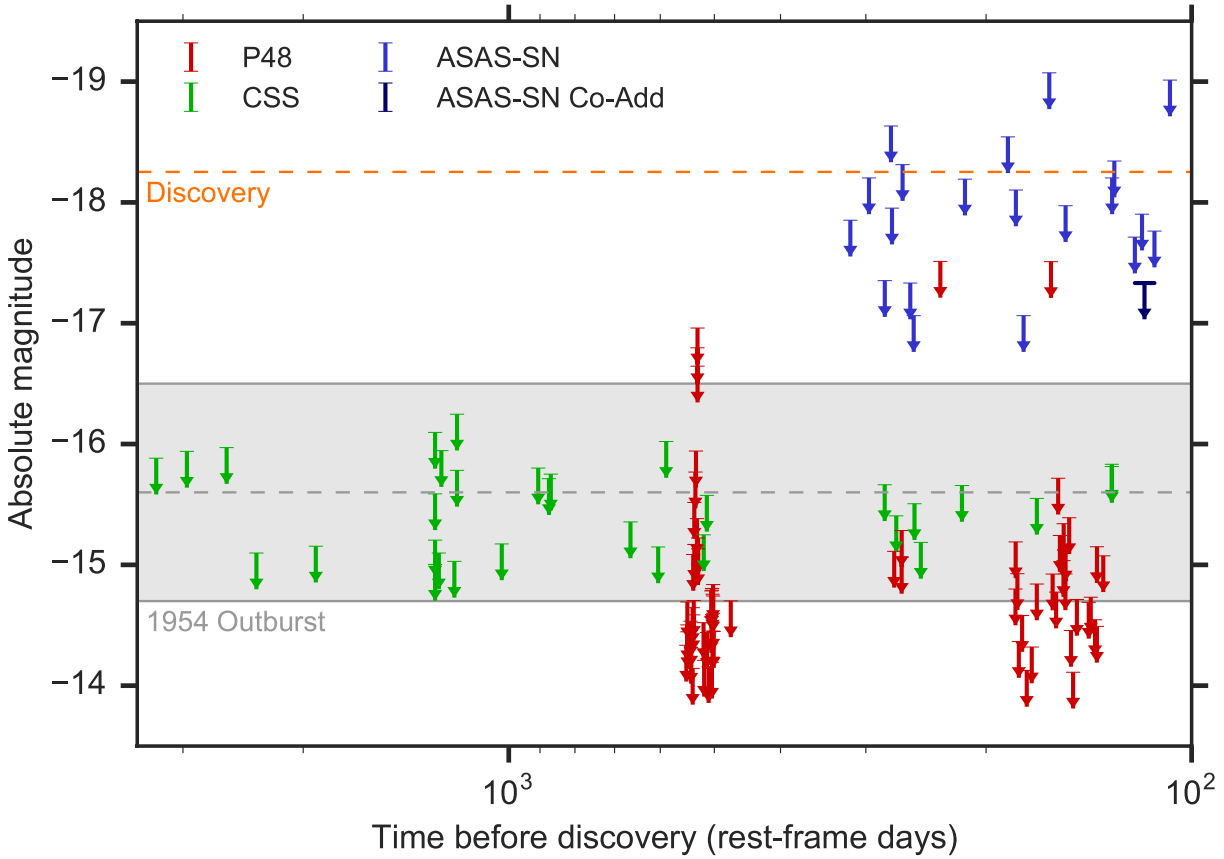

Extended Data Figure 3 | Pre-explosion nondetection limits for iPTF14hls. Data from P48 (*R* band, 3σ nondetections), CSS (unfiltered, obtained via the CSS website), and ASAS-SN (*V* band, 3σ nondetections—the dark-blue arrow is a deep coadd of the three images taken during the time range denoted by the horizontal line in the marker) are shown. The dashed line indicates the discovery magnitude and the shaded region shows the 1954 outburst magnitude and its uncertainty.

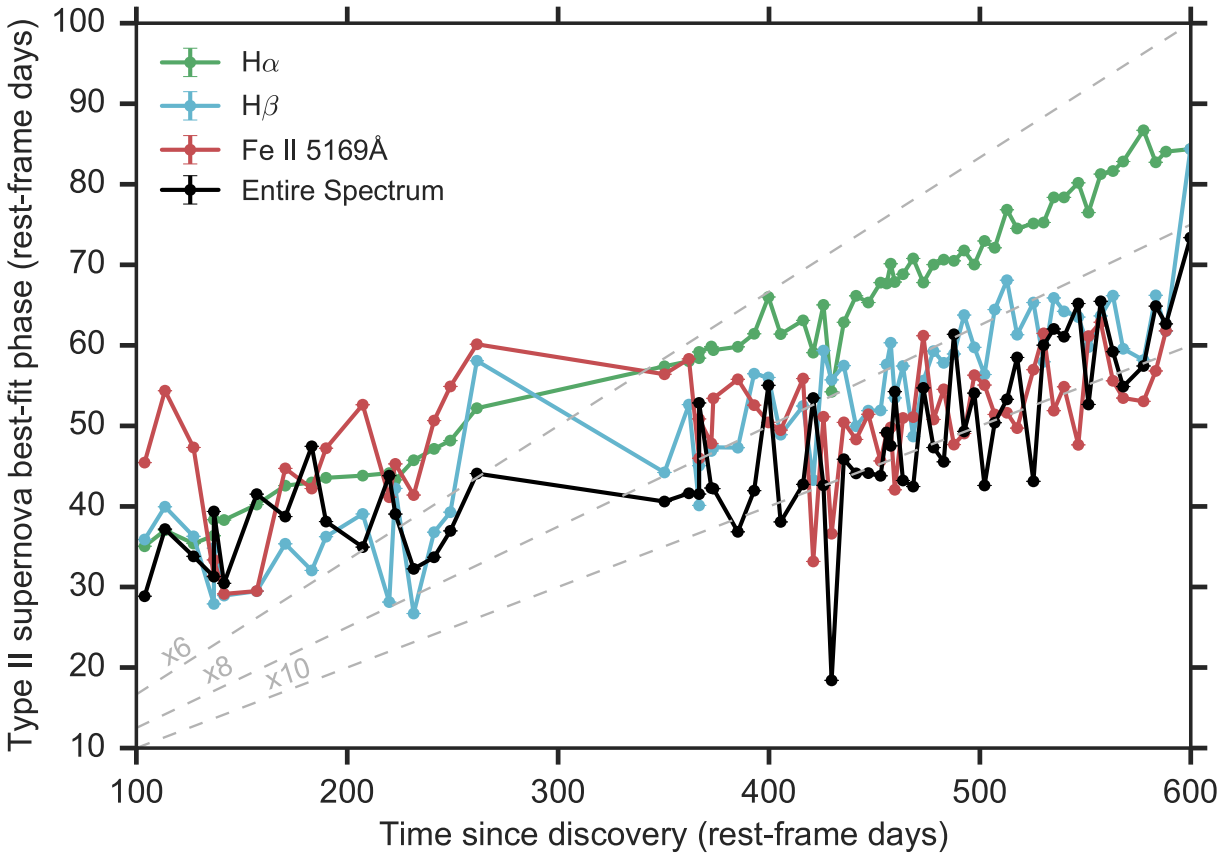

Extended Data Figure 4 | The slow spectral evolution of iPTF14hls compared to normal supernovae. Weighted average best-fit phase of iPTF14hls spectra from Superfit[47], compared to the true spectral phase are shown, when fitting the entire spectrum (black) or only certain line regions as noted. The dashed lines denote constant ratios between the observed and best-fit phases (assuming the explosion happened at discovery). The spectra of iPTF14hls evolve a factor of approximately 6–10 times slower than those of other type II supernovae.

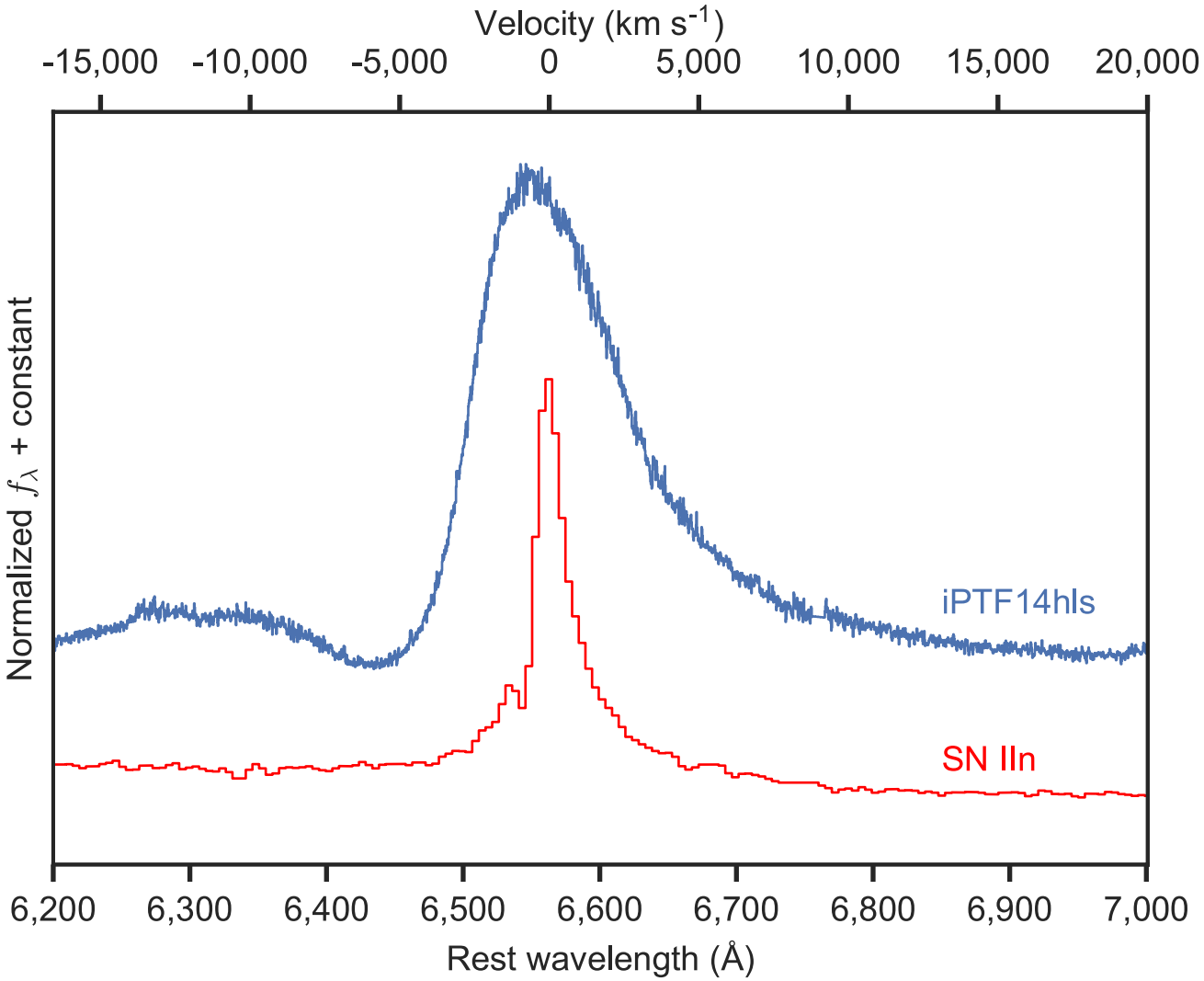

Extended Data Figure 5 | A lack of spectral interaction signatures in iPTF14hls. The Hα region in our highest-resolution spectrum of iPTF14hls taken on 2016 June 4 using DEIMOS on Keck II (blue), expressed in terms of normalized flux density as a function of rest-frame wavelength (bottom axis), compared to the interaction-powered type IIn SN2005cl[18] (red). The top axis is the corresponding velocity of Hα. iPTF14hls shows no signs of the narrow emission or narrow P Cygni features seen in interacting supernovae.

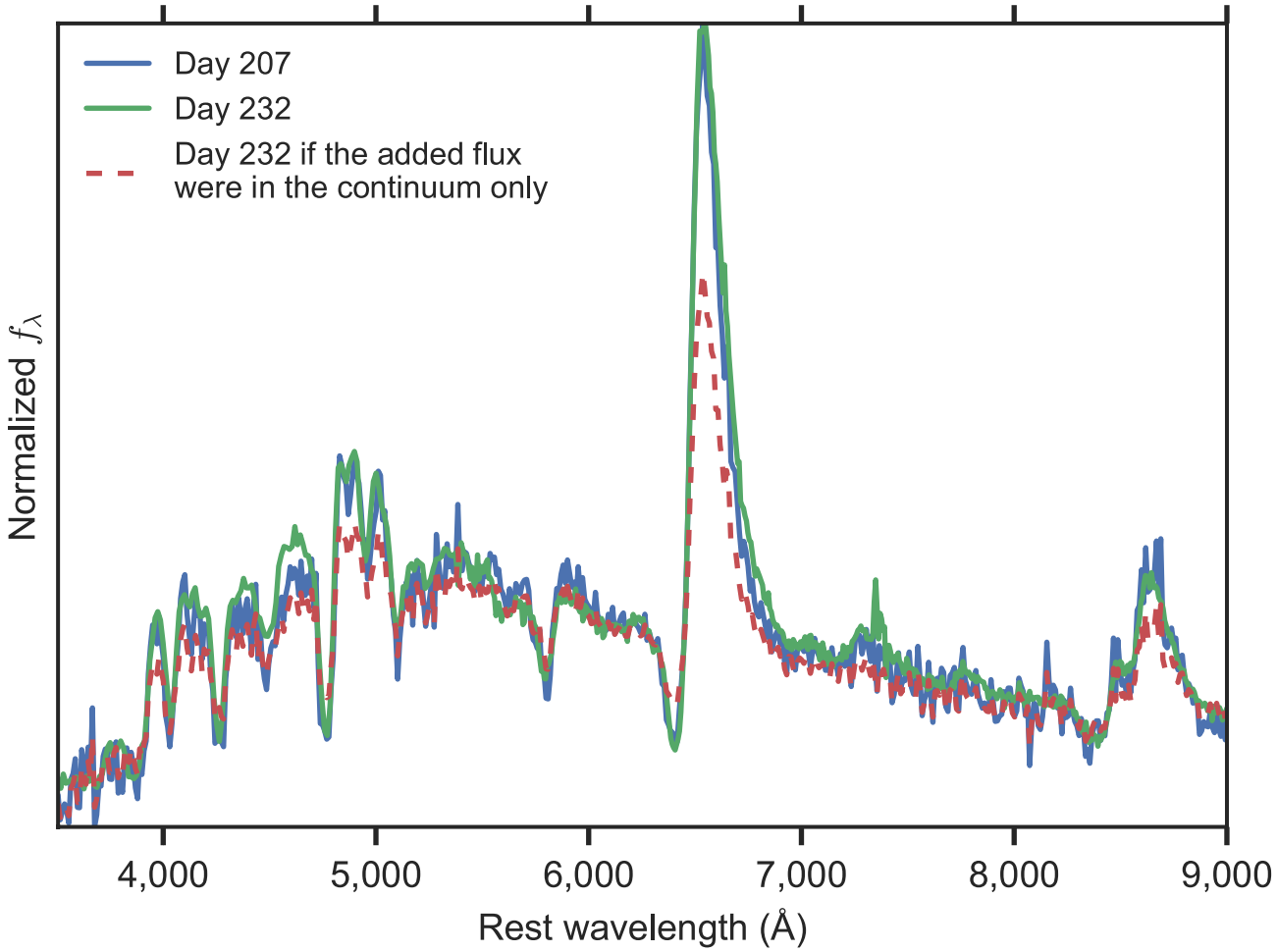

Extended Data Figure 6 | The nature of the increased flux during the brightest peak of iPTF14hls. Spectra of iPTF14hls expressed in terms of normalized flux density as a function of rest-frame wavelength taken on rest-frame day 207 (right before the rise to the brightest peak in the light curve) and day 232 (at the brightest peak in the light curve) after discovery (solid lines) are shown. The similarity of the spectra indicates that the increase of about 50% in luminosity observed in the light curve between the two epochs is equal at all wavelengths. If the increase were due only to the continuum flux, then the line emission on day 232 would have been diluted by the continuum (as simulated by the dashed line).

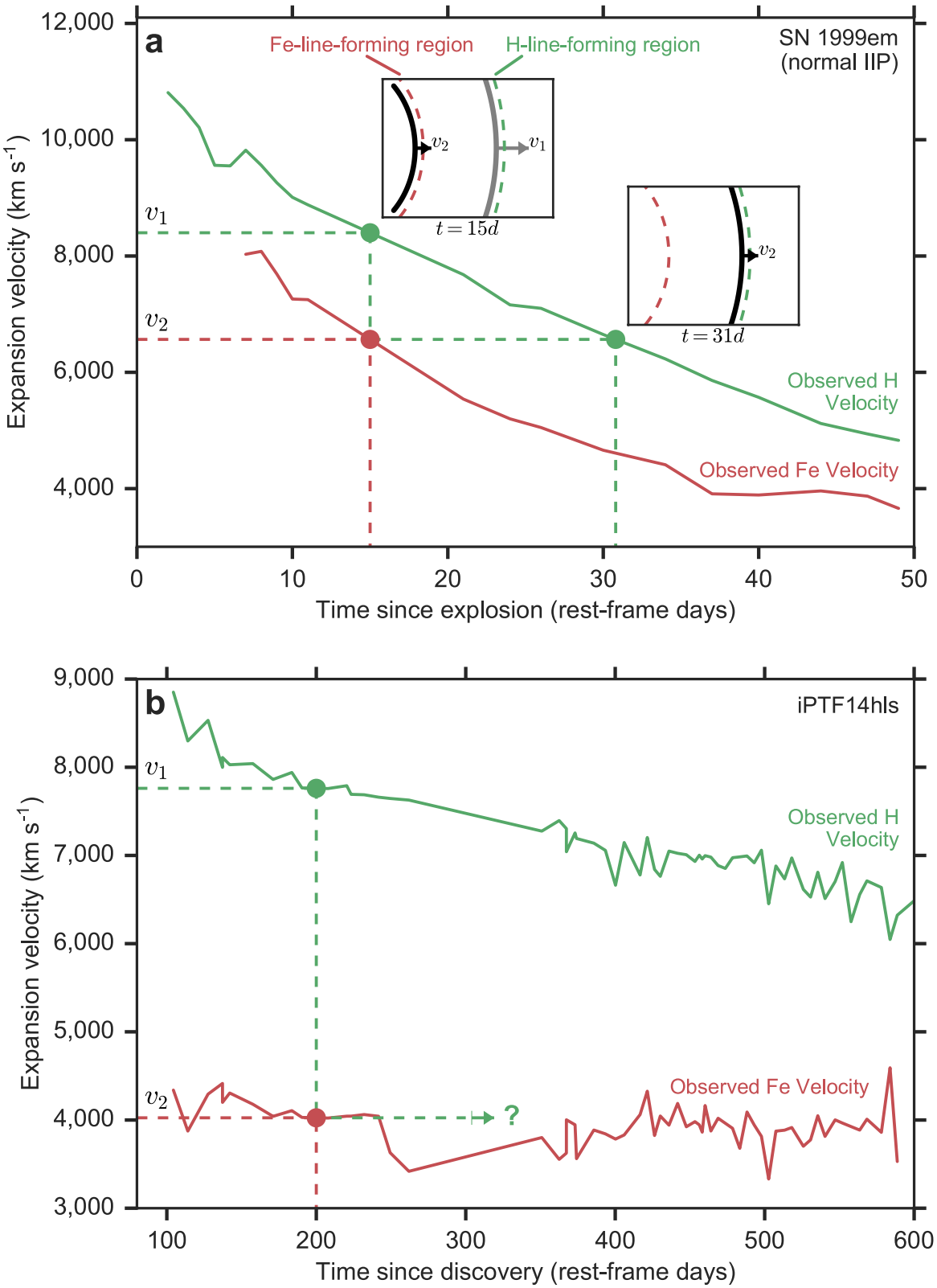

Extended Data Figure 7 | The perplexing velocity evolution of iPTF14hls. Evolution of the measured velocity gradient in the normal type II-P SN 1999em[22] (**a**) and in iPTF14hls (**b**) are shown. At a given time, the H-line-forming region is at material expanding with velocity v_1, while the Fe-line-forming region is at material expanding with lower velocity v_2 (top inset in **a**). For SN 1999em, the H-line-forming region soon reaches the material expanding at velocity v_2 as it moves inward in mass (bottom inset in **a**) and v_2 is measured in the H lines. For iPTF14hls, in contrast, the H-line-forming region does not reach the material expanding at v_2 even after the time since discovery increases by a factor of 6. If the material were ejected at the time of discovery, this would indicate an increase in the radius of the line-forming regions by a factor of about 6, which is unlikely given the observed velocity gradient between the H and Fe lines. If the material were ejected before discovery, on the other hand, the relative expansion in radius would be much smaller, thus offering one possible explanation for the constant velocity gradient observed in iPTF14hls.

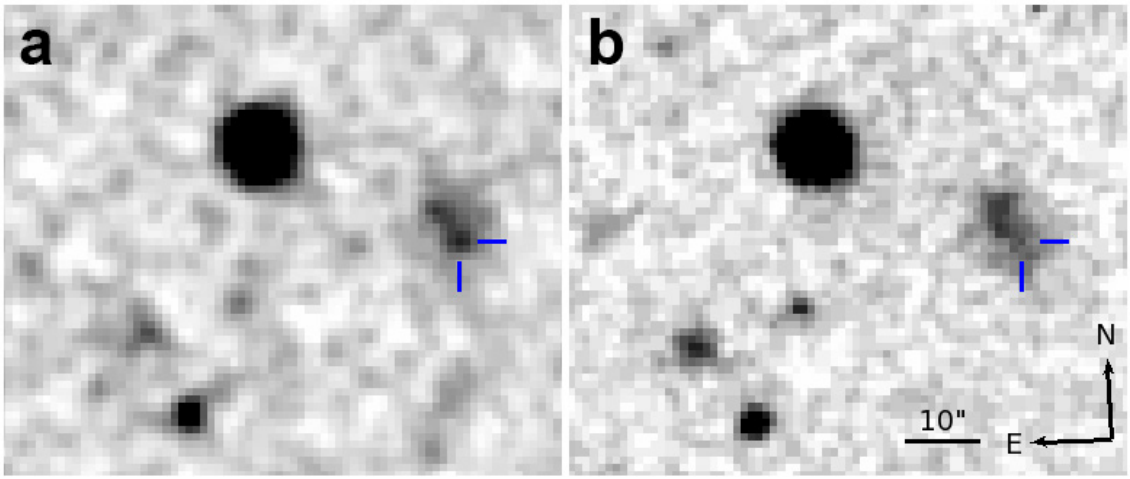

Extended Data Figure 8 | A historic eruption at the position of iPTF14hls. Blue-filter images of the position of iPTF14hls (marked by blue ticks) from 1954 February 23 (POSS; **a**) and 1993 January 2 (POSS-II; **b**) are shown. A source is visible at the position of iPTF14hls in the 1954 image, which is not there in the 1993 image. Using aperture photometry, we find that the 1954 source is 0.31 ± 0.14 mag brighter than the underlying host galaxy at that position, corresponding to a rough outburst magnitude of about -15.6 at the luminosity distance of iPTF14hls, after removing the host-galaxy contribution and calibrating the field to the SDSS $u+g$ bands.

Extended Data Table 1 | iPTF14hls host-galaxy line fluxes

Line	Flux	Flux Error
[O II] 3727 Å	2.050×10^{-16}	1.152×10^{-17}
H**β**	5.666×10^{-17}	6.349×10^{-18}
[O III] 4958 Å	1.742×10^{-17}	6.130×10^{-18}
[O III] 5007 Å	1.003×10^{-16}	6.171×10^{-18}
H**α**	1.539×10^{-16}	4.089×10^{-18}
[N II] 6583 Å	1.361×10^{-17}	4.095×10^{-18}

Data are shown in erg s^{-1} cm^{-2}. Errors denote 1σ uncertainties.

Extended Data Table 2 | iPTF14hls host-galaxy metallicity values

Diagnostic	Metallicity	Lower Error	Upper Error
N06-N2[74]	8.339	-0.126	+0.098
N06-R23[74]	8.633	-0.166	+0.071
D02[75]	8.334	-0.166	+0.139
PP04-N2Ha[76]	8.250	-0.059	+0.044
PP04-O3N2[76]	8.309	-0.051	+0.037
M08-N2Ha[77]	8.458	-0.116	+0.076
M13-O3N2[78]	8.252	-0.035	+0.025
M13-N2[78]	8.249	-0.078	+0.060
KK04-N2Ha[79]	8.490	-0.127	+0.080
KD02comb[80]	8.386	-0.130	+0.055

Data are shown as $12 + \log(O/H)$ values under different diagnostics and calibrations from refs 74–80. Error ranges denote 1σ uncertainties.